RHESSI Hard X-Ray Imaging Spectroscopy of the Large Gamma-Ray Flare of July 23, 2002

A. Gordon Emslie[1], Eduard P. Kontar[2], Säm Krucker[3] & Robert P. Lin[3]

ABSTRACT

We present RHESSI hard X-ray images in different energy bands for the large X-class flare of July 23, 2002. These data are then used to construct spatially-resolved hard X-ray spectra for each of four prominent features evident in these images. These four main features are a bright, low-energy (soft spectrum) source high in the corona, two localized high-energy (hard spectrum) footpoints in opposite polarity magnetic regions that show highly correlated flux and spectral variations in time, and a third footpoint bounded by the other three sources. The power-law spectral indices of the two correlated footpoints differ by $\sim 0.3 - 0.4$. We investigate the possibility that this difference is due to differing column densities from the electron source.

Subject headings: Sun: flares, Sun: X-rays

1. Introduction

Hard X-ray emission has long been recognized as a key diagnostic of the energetic electrons that are accelerated during a solar flare. Numerous analyses, both observational and theoretical, have been made of *spatially-integrated* solar flare hard X-ray spectra, and indeed such analyses can still yield valuable insight into the role of accelerated electrons in the flare (e.g., Holman et al. 2003; Kontar et al. 2003). One of the key features of RHESSI, however, is the ability to synthesize *images* in different energy bands and so determine the hard X-ray spectrum at different locations in the flare volume. Such imaging spectroscopy

---

[1]Department of Physics, The University of Alabama in Huntsville, Huntsville, AL 35899, USA `emslieg@uah.edu`

[2]Department of Physics & Astronomy, The University, Glasgow G12 8QQ, UK `eduard@astro.gla.ac.uk`

[3]Space Sciences Laboratory, University of California at Berkeley, Berkeley, CA 94720, USA `krucker@ssl.berkeley.edu`, `rlin@ssl.berkeley.edu`

capabilities (Lin et al. 2002) significantly exceed those of previous hard X-ray imaging instrumentation, such as the Hard X-ray Telescope (HXT) on *Yohkoh* (Kosugi et al. 1991), both in terms of spectral resolution and Fourier-plane coverage. As shown by Emslie, Barrett, & Brown (2001), imaging spectroscopy analysis of RHESSI data in principle provides a means of determining electron acceleration and transport processes *empirically*.

In this *Letter*, we present imaging spectroscopy results from RHESSI for the large (GOES Class X4.8) flare of July 23, 2002. The data for this study consists of the hard X-ray emission from $\sim$ 00:27:00 UT through 00:39:00 UT, which was the period of main hard X-ray emission for this event. A complete analysis of this fascinating data set is beyond the scope of the present article; we here restrict our discussion to a description of the evolution of the hard X-ray spectrum in each of four relatively long-lived prominent features within the flare.

2. Experimental Details

Imaging spectroscopy using RHESSI is accomplished by making photometric images over a specified time interval in different photon energy bands and then using these images to determine the intensity as a function of energy in different spatial regions (Hurford et al. 2002). The top panel of Figure 1 shows the time profile of the hard X-ray emission in the energy range 60-120 keV for the July 23, 2002 event, divided into nine time segments as illustrated. Each of these time intervals avoids times of attenuator (shutter) movement, which make the determination of both images and spectra difficult.

Smith et al. (2002) and Kontar et al. (2003) have summarized the issues (e.g., decimation, pulse pileup, detector response, background subtraction) that must be considered in the conversion of raw count rate data to photon spectra. For an intense flare, pulse pileup (for RHESSI this requires two photons to interact in a detector within $\sim 0.8\mu$s; this will be incorrectly recorded as a single photon with energy equal to the sum of the individual photon energies) are particularly important for RHESSI's rotating modulation collimator imaging technique (see Lin et al. 2002). The basic information used for imaging (and hence imaging spectroscopy) consists of count rates which may exhibit large variations on small fractions of the $\sim$ 4-second satellite rotation period. Since the number of pulse pileup events is proportional to the square of the observed count rate (Smith et al. 2002), the pileup correction factor varies greatly with time. In this preliminary study we do not use the energy range from $\sim 25 - 50$ keV where pileup is significant (see §2).

In this analysis the counts were binned into energy channels with widths scaled approximately logarithmically with energy. The imaging was done using grids from #8 down to
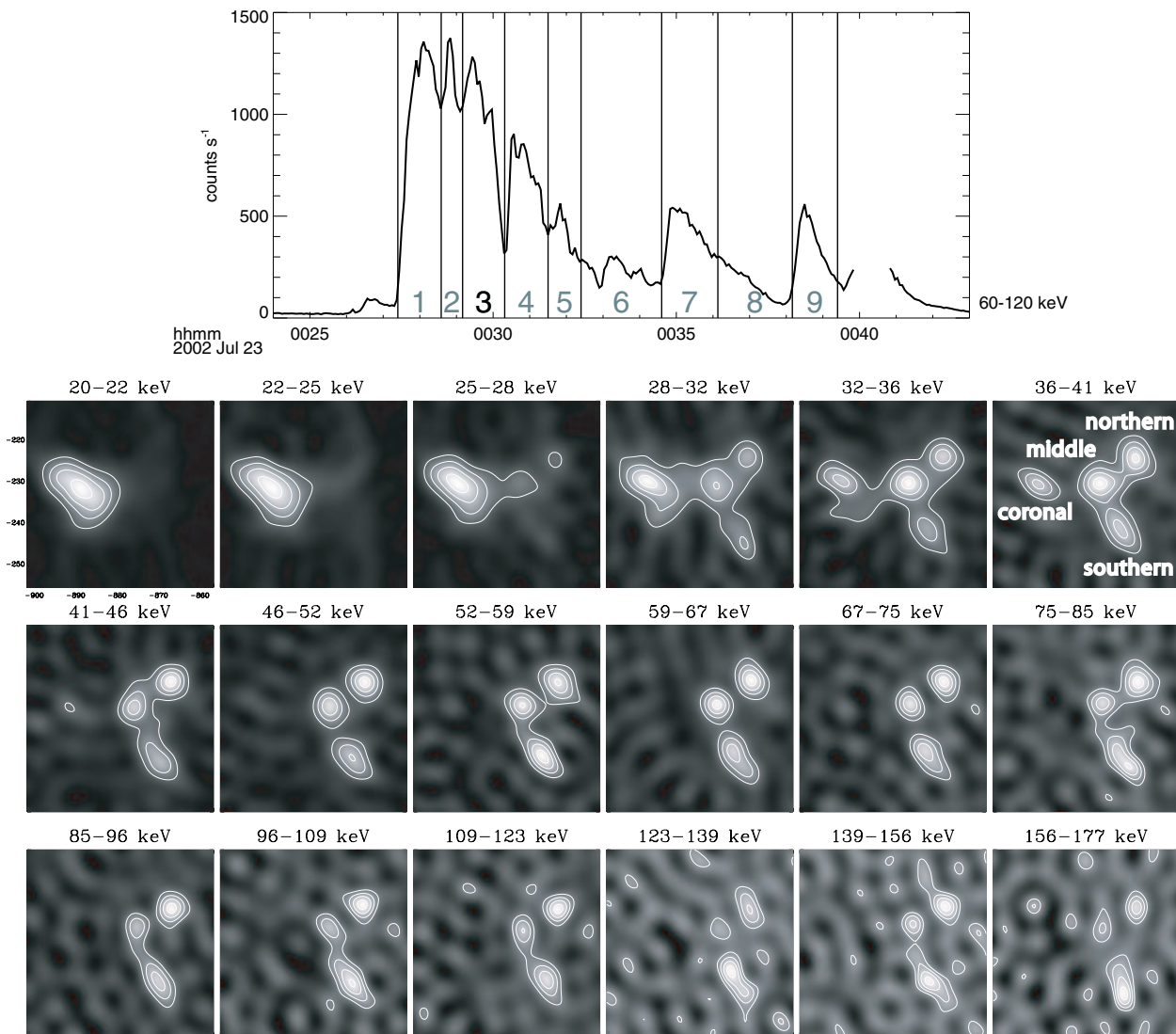
Fig. 1.— *Top panel:* Time profile of the spatially-integrated hard X-ray emission (60-120 keV). Nine time intervals are labelled. *Bottom panel:* CLEAN images for time interval # 3 in several energy bands. The images are centered on the point (-880,-235) [arc seconds in a cartesian Sun-centered coordinate system] and extend ±23 arc seconds in each direction. The direction of Sun center is to the right and slightly upward; the Eastern solar limb lies to the left of the sources. The four main emission regions (coronal source, northern footpoint, southern footpoint, and middle source) have been annotated on the image for the 36-41 keV energy band.

#2. Weighting the grids uniformly gives a spatial resolution of 4.8 arc seconds and allows us to clearly separate the different sources involved; this is crucial for imaging spectroscopy using CLEANed images to avoid contamination of relatively weak sources by the wings of stronger sources. In this analysis, the spectrum was obtained for each of the four (see §3) main sources. Uncertainties in these spectra were derived using the CLEAN residual maps: the ratio of the source maximum to the largest side lobe (i.e. the maximum in residual map) was used as a rough measure of the $\sim 5\sigma$ level. This is a good approximation for point sources, but overestimates the uncertainties of extended sources.

3.   Source Features and their Spectra

Figure 1 shows the images, in sun-centered Cartesian coordinates for time interval number 3 (00:29:10-00:30:19 UT). The images were processed using the CLEAN algorithm, using the default parameters appropriate to Release Version 8.0 of the RHESSI software tree; 0.5 arc-second pixels were used in the image construction. (When analyzing the "coronal" source, with its relatively soft spectrum [see Figure 1], we used only detectors #3 through #8, because of the fairly high ($\sim 20\,\mathrm{keV}$) energy threshold of detector #2; the resulting degradation of angular resolution [to ~ 7 arc seconds] is not critical for this extended [~ 15 arc second] source.) The contours show the 30%, 50%, 70% and 90% intensity levels for each image.

The emission at low energies ($\lesssim 30$ keV) is dominated by a source with a centroid around (-890, -230); this source is located at the greatest distance from the Sun center and is interpreted, both because of its (projected) location and its much softer spectrum (see below) as a coronal source. At higher energies three other features become evident. There are two conspicuous bright sources, one centered around (-865, -225) (which we term the "northern footpoint") and one centered around (-870, 240) ("southern footpoint"). In the middle energy ranges ($\sim 30 - 50$ keV) there is an additional bright feature located around (-875, -230). All four source regions are labelled on the 36-41 keV image in Figure 1.

Figure 2 shows the photon spectra for each of the four main sources identified above, for each of the 9 time intervals used in the analysis, together with the uncertainty level, determined by the procedure discussed in §2. Since side lobes in the CLEAN images, and therefore spectral uncertainties, are larger for relatively complex images, the relative uncertainty levels are smallest during time interval 9 (despite the lower count rate during this interval – Figure 1), because only footpoint sources N and S are present and the coronal source C has decayed significantly.

For some time intervals, some of the sources – most notably the "middle" region M –
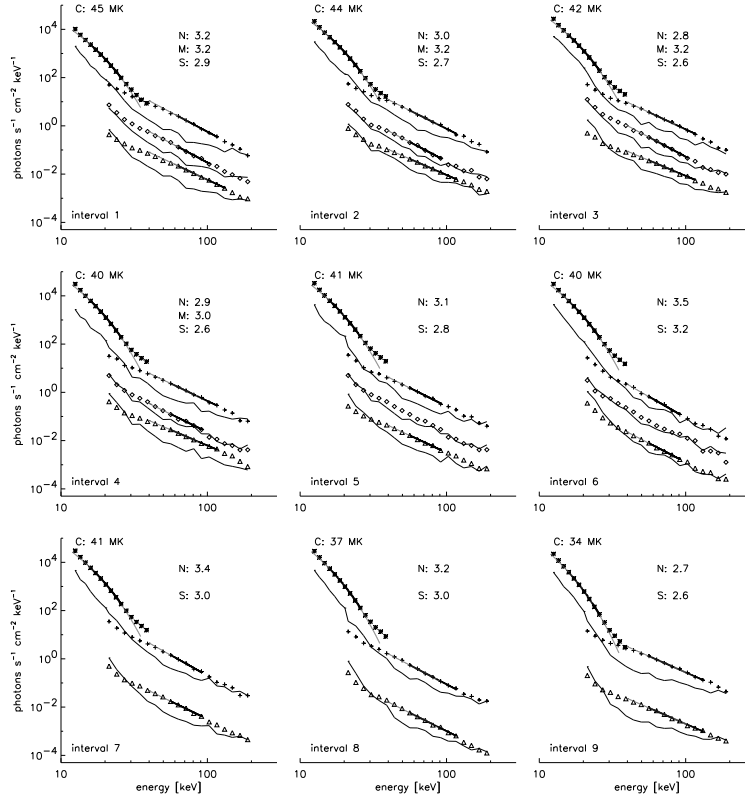
Fig. 2.— Photon spectra for each of the 4 main spatial features: C, coronal source (asterisks), N, northern footpoint (plus signs); M, middle source (diamonds); and S, southern footpoint (triangles). The thin lines represent the uncertainty levels; where these were relatively large the spectrum was not plotted and/or points were excluded from the spectral fits. The spectra for sources C and N are absolute; those for regions M and S have been multiplied by 0.1 and 0.01, respectively, for ease of presentation. The thick black solid lines show best-fit thermal (source C), or power-law (sources N, M and S), spectra; extensions to these fits are shown as solid gray lines. The figures are labeled with the values of T or γ, as appropriate, for each region.

are too faint for a reliable determination of the spectrum and so are not shown. At present, the dynamic range of the RHESSI instrument allows sources down to ~ 0.1 of the intensity of the brightest source present to be accurately determined by the imaging algorithm (this instrumental limitation will be improved in the future as in-flight calibrations become better). Therefore, the spectra of sources N, M and S are uncertain at low energies ($\lesssim 25$ keV); similarly, the spectrum of the coronal source C is uncertain at high ($\gtrsim 30$ keV) energies.

The spectra for regions N, S and M were fitted with power-law forms, using data points within the range 50-120 keV that are well above the uncertainty level (solid black lines in Figure 2). The spectrum for the coronal source C was fitted with a Maxwellian (with emission measure EM and temperature T) over the range 15-25 keV, thereby avoiding pulse pileup and contamination from the other 3 (harder) sources. Each fit in Figure 2 is labelled with the value of $\gamma = -\mathrm{d}\log(I[\epsilon])/\mathrm{d}\log(\epsilon)$, or T, as appropriate.

Figure 3 shows the temporal variation of the best-fit temperature T (K) and emission measure EM (cm^{-3}) for source C, and power law spectral index γ (sources N, S, and M), over periods when these quantities could be reliably determined. The best-fit values of T, EM and γ for the *spatially integrated* hard X-ray emission (Holman et al. 2003) are superimposed as solid lines.

The coronal source C shows a steadily decreasing temperature T (from $\sim 4.5 \times 10^7$ K to $\sim 3.5 \times 10^7$ K) and an emission measure that initially rises to a value $\sim 10^{49}$ cm^{-3} at $\sim$00:30 UT and then slowly increases by a factor of ~ 2 thereafter. Both the temperature and emission measure show a temporal behavior that is similar to that of the spatially-integrated emission. However, the value of T for the coronal source is some 5 million degrees larger than for the flare as a whole and 15 million degrees larger than the maximum temperature (~ 30 million K) deduced from GOES soft X-ray data; similarly the emission meaure of source C is less than that for the spatially-integrated emission and even less than the $\sim 4 \times 10^{49}$ cm^{-3} deduced from GOES data (Holman et al. 2003). This not surprising: the presence of lower-temperature thermal emission outside of source C, which is too weak to be effectively imaged but which nevertheless contributes to the overall emission from the flare, causes the temperature (emission measure) of source C to be larger (smaller) than for the flare as a whole.

The temporal evolution of the spectral indices of the N and S footpoints γ follow each other, showing "soft-hard-soft" (cf. Fletcher & Hudson 2002) behavior through the first burst (intervals 1 through 6), hardening again for the second (interval 7) and third (interval 9) bursts. This is similar to the behavior of the spatially integrated flare emission (Holman et al. 2003). The spectrum for the source M (over the period $\sim$00:28-00:31 UT, when it can be reliably inferred) has a value of γ that is consistently the largest (steepest) of the three; its
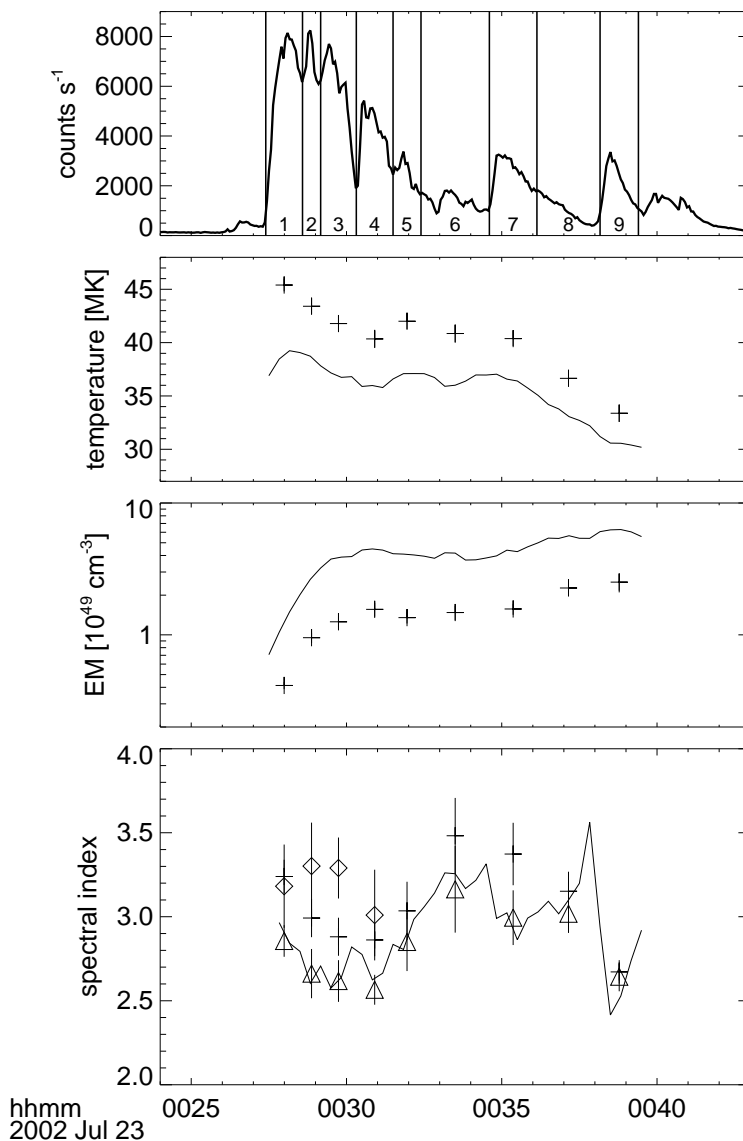
Fig. 3.— Temporal variations of the best-fit temperature T and emission measure EM for the coronal source C, and spectral indices γ for sources N (plus signs), S (triangles), and M (diamonds). Superimposed are the best-fit values of T, EM and γ for the spatially-integrated emission, as calculated by Holman et al. (2003). (Note that γ cannot be reliably calculated for source M after 00:31 UT, because of its faintness at these times.)

variation with time appears to differ from the N and S sources, although the uncertainties are large.

4. Discussion

RHESSI hard X-ray imaging spectroscopy of the July 23, 2002 event has shown that the hard X-ray emission is concentrated in four main features – a coronal source C with a steep spectrum, and three footpoints: (N and S) with relatively hard spectra, and a "middle" source M with a spectrum similar to, but consistently somewhat steeper than, those of footpoints N and S. The spectrum of the coronal source is consistent with a thermal source with a temperature $T \simeq 40 \times 10^6$ K and generally follows the temporal trend for the spatially-integrated thermal emission; the spectral indices of the footpoint features also follow that of the spatially-integrated nonthermal high-energy emission. Sources N, S, and M appear to be chromospheric footpoints, since they each have counterparts seen in EUV and Hα, and in the SoHO MDI observations (Krucker, Hurford & Lin 2003).

Since the N and S footpoints are in opposite polarity magnetic fields, and their X-ray fluxes are closely correlated (Krucker, Hurford & Lin 2003), we identify them as opposite ends of a coronal loop. The correlated temporal variations of the two sources is consistent with this picture. Figure 3 shows that the spectral index of footpoint S is systematically less than that at footpoint N by an amount $\gamma_N - \gamma_S \simeq 0.3 - 0.4$ from the start through interval 7. Such a spectral difference would result if the column density at the top of the chromosphere at footpoint S were greater than that at footpoint N, so that Coulomb collisions harden the incident electron spectrum by a greater amount. For Coulomb collisional degradation, the energy E at column depth ξ (cm^{-2}) is given by $E^2 = E_o^2 - 2K\xi$, where $K = 2\pi e^4 \Lambda$, e being the electronic charge and Λ the Coulomb logarithm $\simeq 25$. For a power-law injection spectrum $F_o(E_o) \sim E_o^{-\delta}$, the local electron flux is, by flux continuity, $F(E, \xi) \sim E\left(E^2 + 2K\xi\right)^{-(\delta+1)/2}$, so that the integrated bremsstrahlung emission below column depth ξ at photon energy ϵ is given by

$$J(\epsilon, >\xi) \sim \frac{1}{\epsilon} \int_\epsilon^\infty \int_\xi^\infty \frac{F(E, \xi)}{E} \, d\xi \, dE \sim \frac{1}{\epsilon} \int_\epsilon^\infty \int_\xi^\infty \left(E^2 + 2K\xi\right)^{-(\delta+1)/2} d\xi \, dE, \qquad (1)$$

where the Kramers bremsstrahlung cross-section $Q \sim 1/\epsilon E$ has been used for simplicity. Evaluation of this expression yields the result

$$J(\epsilon, >\xi) \sim \frac{\xi}{(\delta - 1)} \frac{1}{\epsilon} \left(2K\xi\right)^{-\delta/2} B\left(\frac{\delta}{2} - 1, \frac{1}{2}; z\right), \qquad (2)$$

where $B(a, b; z)$ is the incomplete beta function and $z = (1 + \epsilon^2/2K\xi)^{-1}$.

We used the above expression to derive footpoint photon spectra for various values of ξ. We then determined the best-fit spectral index γ over the photon energy range from 50-120 keV (cf. Figure 2). The best-fit γ shows a steady decrease with increasing ξ due to collisional hardening of the exciting electron beam; for plausible (chromospheric) values of $\xi \simeq 10^{20} - 10^{21}$ cm^{-2}, the rate of change of γ is approximately one per decade in column density. To produce a difference in γ of order 0.3 (cf. the values of γ_N and γ_S in Figure 3) therefore requires a ratio of column densities at the top of the chromosphere of ~ 2, with the column density of the harder source (S) being larger. This additional column density between the acceleration region and source S could be due to several factors – a location of the acceleration region farther from source S, a greater density in the leg of the loop toward source S, or a greater pitch angle for the electrons streaming toward source S.

Figure 3 shows that the spectral index γ of source M is the same as source N at the start, but then becomes $\sim 0.3 - 0.4$ greater. Source M is located in the opposite magnetic polarity region from source N and is not as highly correlated with source N as source S. However, if it is also linked magnetically to source N the difference in spectral index might be accounted for in a similar way.

REFERENCES

Brown, J.C. 1971, Sol. Phys., 18, 489

Brown, J.C. 1973, Sol. Phys., 31, 143

Emslie, A.G., Barrett, R.K., & Brown, J. C. 2001, ApJ, 557, 921

Fletcher, L. & Hudson, H.S. 2002, Sol. Phys., 210, 307

Holman, G.D., Sui, L., Schwartz, R.A., & Emslie, A.G. 2003, ApJ, this volume

Hurford, G.J, and 13 co-authors 2002, Sol. Phys., 210, 61

Kontar, E.P., Emslie, A.G., Brown, J.C., Schwartz, R.A., Smith, D.M., & Alexander, R.C. 2003, ApJ, this volume

Kosugi, T., Masuda, S., Makishima, K., Inda, M., Murakami, T., Dotani, T., Ogawara, Y., Sakao, T., Kai, K. & Nakajima, H. 1991, Sol. Phys., 136, 17

Krucker, S., Hurford, G.J., & Lin, R.P. 2003, ApJ, this volume

Lin, R.P., and 65 co-authors 2002, Sol. Phys., 210, 3

Mariska, J.T., Emslie, A.G. & Li, P. 1989, ApJ, 341, 1067

Masuda, S., Kosugi, T., Hara, H., Sakao, T., Shibata, K., & Tsuneta, S. 1995, PASJ, 47, 677

Piana, M., Massone, A.M., Kontar, E.C., Emslie, A.G., Brown, J.C., & Schwartz, R.A. 2003, ApJ, this volume

Smith, D. M., and 19 co-authors 2002, Sol. Phys., 210, 33